Supporting Information

Singer et al. 10.1073/pnas.1302295110

SI Methods

Topographical Data Analysis. To characterize historical changes in topography, longitudinal (thalweg) and cross-section profiles were extracted and compared from 1906 California Debris Commission maps (1) and 1999 LiDAR tied to photogrammetry and sonar data by the US Army Corps of Engineers (2, 3). The mean horizontal root-mean-square error associated with georegistration of the four 1906 map sheets was 5.47 m; this is relatively high for georegistration of historic paper maps, which required mosaicking of panels with limited cultural features existing in 1906 (4). Supporting data on changes in topography (Table S1) came from an external source (5).

Streamflow Analysis. Streamflow measurements and historical daily discharges at US Geological Survey (USGS) gauging sites along the Yuba River below the Englebright Dam (site 11418000) and near Marysville (site 11421000) were obtained from http://waterdata.usgs.gov/nwis. Historical daily streamflow data at site 11418000 (pre- and postdam) were analyzed for frequency in annual peak discharge, time to peak (rising limb), and drawdown time (falling limb) based on empirical plotting positions (6), and the data were compared using the Kolmogorov–Smirnoff (K-S) statistic in MATLAB (MathWorks). These aspects of hydrograph shape provide insight into changes in the duration of flood events capable of infiltrating banks and terraces. Graphical differences in the values for rare floods are evident, even when the overall distributions are not significantly different (e.g., drawdown time). Statistics include annual flood peak (K-S = 0.378; $P = 0.007$), time to peak (K-S = 0.151; $P = 0.028$), and drawdown time (K-S = 0.097; $P = 0.344$). Although there is a significant difference between pre- and postdam annual flood peaks (mostly decreased in the postdam period), there do not appear to be differences for the largest floods. In contrast, there are no significant differences in rising or falling limb duration, even though there appear to be marked increases in both for the largest floods. Changes in bed elevation in Fig. 1 for the early 20th century were obtained from Gilbert (7).

Recent changes in bed elevation (incision) were computed using streamflow measurements during relatively low streamflow (Q) from USGS gauging stations to obtain internally consistent values of riverbed elevation (BE):

$$BE = h - \left(\frac{A}{w}\right),$$

where h is measured flow stage, A is flow area, and w is flow width, assuming a rectangular cross-section (8). These individual values of BE_i, where subscript i indicates an individual value of BE, were then differentiated to obtain cumulative change in bed elevation (BEC) from the time series, which was annualized to obtain the values presented in Fig. 1:

$$BEC = \sum_i BE_i - BE_{i-1}.$$

Sediment and Geochemical Analyses. Sediment samples were extracted from bank exposures at field-identified sedimentary units along vertical sections spanning the area from the Englebright Dam to the lowland Central Valley, including deposits along the Yuba, Feather, and Bear Rivers (Fig. 1). We obtained 176 samples from 105 locations, including several samples at banks/terraces within stratigraphy and individual samples on channel bars (Fig. 5*A* and Table S1). Samples in stratigraphy were noted in terms of their superposition (which layers were above other layers) and in terms of their geomorphic units. All sediment samples were sieved through <63-μm stainless-steel sieves to compare total Hg concentration (HgT) in a common sediment population across all sites. Furthermore, it has been shown that particles in this fine-grained fraction tend to adsorb most of the Hg (9, 10). The resulting material was digested in Teflon bombs with aqua regia and BrCl (11) in a class 1000 clean room at the USGS in Menlo Park, California. Digested samples were harvested and analyzed on a Tekran Series 2600 Automated Mercury Analysis System, a cold vapor atomic fluorescence spectroscopy detector. We used dual-stage gold preconcentration and $SnCl_2$ reduction according to standard procedures (US Environmental Protection Agency method 1631). International Atomic Energy Agency (IAEA) 405 (estuarine sediment) was used as certified reference material. Detection limits are <0.02 ng/L. For analysis of the ^{137}Cs and ^{210}Pb fallout radionuclides, samples were dried, ground, and packed into counting containers to match a calibrated geometry. Activities were determined in the Exeter Radiometry Laboratory with High-Purity Germanium (HPGe) spectrometers (Ortec LO-AX and GMX) featuring ancient lead shielding, digital electronics, and efficiency corrections to account for density variations. Zr and Ni were measured via Inductively Coupled Plasma Mass Spectrometry (ICP-MS) at Activation (ACT) Laboratories Ltd. and the Centre for Earth Resources at the University of St. Andrews. HgT data presented in Fig. 5 include all analyzed samples, comprising individual samples for bar or channel sediments (squares) and each of those extracted from multiple stratigraphic layers within historical terraces (circles). Thus, for many locations (i.e., distances downstream from the fan apex), multiple values of HgT are presented, producing scatter in the downstream trend. We did not integrate or aggregate HgT values. All HgT values are listed in Dataset SI, where sample codes indicate the position within stratigraphy. The letters (A, B, C, etc.) at the end of the sample code indicate the position within stratigraphy (alphabetically sorted from top to bottom layer).

Erosion Modeling. Physically based terrace erosion modeling was conducted at an indicative river valley cross-section bounded by large terraces (>17 m high) near the fan apex (Fig. 2*A*), using an adaptation of the infinite slope stability model for riverbanks (12). This model tracks the relationship between river flow stage and flow through porous media in the bank/terrace to compute a factor of safety (FoS) at quarter hourly time steps. The terrace/bank is divided into a series of vertical columns, and we assume the water surface elevation in the bank column abutting the channel is equal to that of the river. Water draining from and seeping into the bank is then calculated via 1D implementation of the Richards equation (for flow through a porous medium under unsaturated conditions) through the bank columns using the Dupuit–Forchheimer assumption (flow moves horizontally between columns, assuming no infiltration recharge from above or loss below): $\frac{\partial h}{\partial t} = \frac{K}{\varepsilon} \cdot \frac{\partial}{\partial x}\left(h \cdot \frac{\partial h}{\partial x}\right)$, where h is water surface elevation, t is time (time step is 15 min), K is permeability, ε is porosity, and x is distance into the terrace. The calculations of FoS include weight of the failure material block taking into account the degree of saturation (from the Richards equation); hydrostatic uplift force (positive pore-water pressure in the saturated zone) (13); confining pressure; suction force (negative pore-water pressures from matric suction in the unsaturated zone) (13); and effective cohesion, based on a homogeneous characteriza-

tion of bank materials. The *FoS* is determined as the ratio between the physical resisting forces (F_r) and the forces driving bank erosion (F_d):

$$FoS = \frac{F_r}{F_d}. \quad \textbf{[S1]}$$

The resultant driving force is

$$F_d = F_w \sin\beta - F_{cp} \sin\delta, \quad \textbf{[S2]}$$

where F_w is the weight of a unit width of the failure block (newtons per meter), β is the angle of failure plane (degrees), F_{cp} is the hydrostatic confining pressure (newtons per meter), and δ is the angle between the resultant of the hydrostatic confining pressure and the normal vector of the failure plane (degrees). This angle is computed based on water surface elevation from the Dupuit–Forchheimer equation. The resultant resisting force is

$$F_r = c'L + F_{suc} + \left(F_w \cos\beta + F_{cp} \cos\delta - F_{hu}\right)\tan\phi',$$

where c' is the effective cohesion averaged across each individual riverbank soil layer (kilopascals); L is the length of failure plane (meters), which is calculated trigonometrically based on the bank height; F_{suc} is the suction force due to negative pore-water pressure (newtons per meter), F_{hu} is the hydrostatic uplift force due to positive pore-water pressure (newtons per meter), and ϕ' is the angle of internal friction (degrees). F_{suc}, F_{hu}, and F_w are computed using water surface elevation output from the Dupuit–Forchheimer equation above, and F_{cp} is computed based on flow stage in the channel. More details on the model structure can be found in the article by Amiri-Tokaldany et al. (14). Parameter values for the model are listed below.

There is no substantial vegetation present in this environment, and no tension cracks were visible during an on-site survey, so such effects are excluded. Once the model identified terrace failure, we quantified the volume of the failed material (based on the column width of terrace at which the calculated FoS value is lowest), and the grain size distribution (GSD) of the riverbed material was updated based on percentage cover of the channel bed by failed material at the field-measured angle of repose at the bank toe. In other words, we compute the volume of failure and then drape it on the terrace toe at the angle of repose, determine what percentage of the channel bed it covers, and update the GSD for the whole cross-section based on this percentage contribution (4% for one-column fail, 12% for two-column fail, and 24% for three-column fail).

Relevant modeling parameters used include bank height = 16.7 m, terrace angle = 75°, and terrace toe angle = 33°, all based on field survey via laser range finder, and internal angle of friction = 38°, porosity = 30%, and permeability = 0.001 m/s, all based on values reported by Selby (15) for our measured terrace GSD (presented below). Effective cohesion was set to 100 kPa based on the value for clay (15), even though the terrace is composed of sand and gravel. This was because we noted chemical cementation of the terrace material in the field that afforded it more stability than would be typical for such materials. Column widths were set to 20 cm to accommodate the largest grain diameter measured in the field, and we computed slope stability for each column width separately. The measured GSDs in the terrace were as follows (fractions in each size class, followed by sieve diameters in parentheses): 0.01 (0.063 mm), 0.01 (0.125 mm), 0.04 (0.25 mm), 0.15 (0.5 mm), 0.09 (1 mm), 0.07 (2 mm), 0.08 (4 mm), 0.12 (8 mm), 0.18 (16 mm), 0.19 (32 mm), and 0.06 (64 mm). Flow data used to drive the hydrological model for each major flood event were extracted from USGS gauging records (*SI Methods*, *Washload Flux Modeling*).

Because the study was concerned with fine-sediment flux from terraces, we assumed no topographical changes to the cross-section. Grain sizes were measured in the field in detail at this site. The measured GSDs in the bed (based on bar sampling) were as follows (fractions followed by sieve diameters in parentheses): 0.06 (2 mm), 0.14 (4 mm), 0.12 (8 mm), 0.15 (16 mm), 0.31 (32 mm), and 0.22 (64 mm). Bed material sediment flux was computed iteratively for the cross-section, based on updated grain sizes and daily flow stage in the channel by the Singer–Dunne equation (16): $qs_n = \alpha \frac{\rho_s U^2 (\tau^* - \tau_c^*)\sqrt{\tau_c^*}\sqrt{\left(\frac{\rho_s}{\rho} - 1\right) g d_n^3}}{2gHS} f_n$, where qs_n is the unit bed material transport rate (kilograms per second) per meter of width of size class n, α is a dimensionless grain size-dependent parameter computed based on the GSD, ρ_s is the density of sediment (assumed to be 2,650 kg·m^{-3}), U is the streamwise velocity (meters per second) computed via an empirical fit of the Darcy–Weisbach formula based on bed grain size (17), τ^* is the dimensionless shear stress for d_{50}, τ_c^* is the dimensionless critical shear stress for d_{50} (assumed to be 0.045), τ_n^* is the dimensionless shear stress computed for a particle in size class n, ρ is the density of water (assumed to be 1,000 kg·m^{-3} for water at 10 °C), g is the gravitational acceleration (9.81 m·s^{-2}), d_n is the characteristic grain size (meters) of the size class for which the computation is being made, f_n is the fraction of bed material in that grain size class, H is the channel flow depth (meters), and S is the water surface slope. This equation is fractional (computes flux for each size class) and is sensitive to bed material GSDs (18). Flux calculations were based on cross-section hydraulics, assuming steady uniform flow. Instantaneous fluxes were summed for each flood event to obtain hind-cast estimates of fine sediment flux transported through the cross-section. This modeling strategy represents the partitioning of eroded terrace sediment into bedload and suspended load that occurs upon bank/terrace failure. The analysis, done for a single cross-section in the Upper Fan (Fig. 2*A*), where there is field and photographic evidence of past terrace failure, is indicative of the links between bank/terrace erosion and downstream sediment flux, and thus provides constraints on the flux of fine sediments during large floods.

Washload Flux Modeling. Fine sediment load in California's Central Valley has been shown to be important in affecting conveyance capacity in floodways (19, 20), as well as for the net downstream transport of Hg (21, 22). Flood event inundation depths and suspended sediment concentrations in the Yuba River channel and its floodplains were modeled using TELEMAC 2-D (Laboratoire National d'Hydraulique, Paris, France) (23) and Sisyphe (a coproperty of the Centre d'Etudes Maritimes et Fluviales, Université de Technologie de Compiègne, Électricité de France, and the Société Grenobloise d'Études et d'Application Hydrauliques), a finite element hydrodynamic and washload transport modeling approach (24). Suspended sediment input was conservatively approximated as a point source within the Yuba Fan based on a rating curve developed between concentration and discharge from historical data from Yuba River near Marysville (USGS site 11421000). This curve represents a low estimate of sediment supply during large floods because it contains data collected in events smaller than those modeled here. We expect the curve would increase nonlinearly in large events due to the lateral erosion of banks/terraces. Because rating curves are fits between discharge and sediment concentration, we used the error on the slope of this curve to compute uncertainty in sediment loads for each modeled flood event presented in Fig. 4. The error in concentration was propagated by multiplying it by discharge to obtain values of uncertainty in sediment flux at the model boundary. These were summed over the entire hydrograph for each flood event to compute a total flood-event flux uncertainty. Although there is undoubtedly additional uncertainty in washload flux estimates

based on hydrodynamics and interaction with sediment, this is not represented within the uncertainty values in Fig. 4.

These conservative estimates of sediment supply to the Yuba River at this location were routed through the Yuba and Feather Rivers to obtain total fluxes for the events of 1986 (10 d), 1997 (18 d), and 2006 (7 d). Details of the model are described by Kilham (24). Topography was defined using a seamless dataset of sonar channel bathymetry and high-resolution floodplain topography, resulting in a final mesh with an average channel element size of 10 m. Leveed sections defining the model side boundaries were characterized as impassable, and the upstream and downstream boundaries were kept open to allow for fluxes of sediment and water. Inundation depths were determined by solving the depth-averaged St. Venant equations with a resistance parameter characterizing the predominant land cover observed in each floodplain element based on classification of satellite imagery (24). Details of the governing equations can be found elsewhere (www.opentelemac.org/) (23). Sediment transport was accomplished by solving the depth-integrated advection–diffusion equation for a passive scalar (e.g., the particle concentrations). This assumes that the sediment velocity is equal to the mean fluid velocity modified for the effect of vertical settling. Deposition was modeled as a function of the size and weight of the particle, the suspended sediment concentration gradient, and an upward buoyant force dependent on the velocity and acceleration of both the particle and the flow. This approach is based on a definition of deposition by which sediment falls and, most importantly, sticks to the bed (25, 26). Erosion at these floodplain velocities was considered negligible, and it was set to zero. Previous studies on floodplain flow have shown that the shear velocities on lowland river floodplains are generally insufficient to cause erosion or resuspension of recently deposited sediment, except at the beginning of inundation (27). Model parameter values for TELEMAC/Sisyphe included median grain size = 0.03 mm; roughness coefficient (Manning's n) for the channel = 0.035; settling velocity = 0.0078 m/s, based on the Krone formula; sediment density = 2,650 kg/m^3; minimum water level = 0.1 m; water viscosity = 0.0000013 m^2/s; porosity = 37.5%; longitudinal dispersion = 0.6; and transverse dispersion = 6.0.

The modeled concentrations were compared with sediment concentration values observed from space during floods for this area and classified by remote sensing methods (28). Our evidence from spectrally classified Landsat images shows that significant (>100 mg/L) concentrations persisted in the Yuba River 30 d after the peak of the 1986 event (28). As such, our approach provides a conservative estimate of event-based flux.

Per Flood Flux Estimates. We summed the total modeled mass flux (*SI Methods*, *Washload Flux Modeling*) and assumed a sediment bulk density of 1,200 kg/m^3 (based on several field measurements of mining deposits) and average HgT of 0.18 μg/g. The latter is the mean of HgT values from 10 selected samples (set in boldface in SI Dataset 1) from the Lower Feather River and Lower Yuba Fan, representing recent (past several decades) deposition (Fig. 2) determined by ^{137}Cs dating, field observation, and/or analysis of historical imagery. This conservative estimate is equivalent to the Hg concentration of the most recent flood deposits (uppermost stratigraphic layers, Fig. 2). These Hg flux estimates are presented in Fig. 4, and the uncertainties provided are based on the error in assigning the slope of the sediment rating curve (*SI Methods*, *Washload Flux Modeling*), rather than on variability in initial HgT or any parameter sensitivity in TELEMAC. We multiplied the flux uncertainty by the characteristic HgT to obtain the event-based uncertainty in Hg concentration for each flood. Then, the flux as a percentage of the total stored mass was calculated based on the original estimated mass of the Yuba Fan *ca.* 1880 (~252×10^6 m^3). We assume that suspended load comprises 85% of the total sediment load, with bedload flux making up the remaining 15%. Assuming 90% remaining in the fan deposit (29) and one large flood per decade, this yields a per flood total load flux of ~0.09% of the original deposit, thus requiring >10^4 y to evacuate sediment from hydraulic mining. These estimates are conservatively low for several reasons: (*i*) mining sediment is diluted with nonmining sediment by the time it reaches the fan outlet (Fig. 2); (*ii*) following progressive lateral erosion, lateral mining deposits will require progressively large floods to access these sediments; and (*iii*) the mix of grain sizes within the Yuba Fan suggests that a significant proportion of the mining sediment will lag behind the washload export described herein. Indeed, bedload flux rates are probably quite low at the fan outlet due to low water surface slope during flood.

Multipronged Approach. This paper presents the culmination of a multipronged, process-based approach that included assessment of historical topographical datasets, investigation of streamflow measurements at historical gauging stations to determine rates of bed elevation change, analysis of flood frequency, interpretation of chemostratigraphy using historical channel change data (from maps) along with HgT, inference from remotely sensed imagery, Zr/Ni geochemistry as an independent proxy for mining sediment, and ^{137}Cs to establish age control for younger deposits. These approaches were combined with the modeling of terrace erosion by slope stability by taking into account the water table elevation in the terrace, partitioning of failed material into bedload vs. suspended sediment loads, and modeling of flow and suspended flux through the fan. These steps allow us to investigate dilution of a particular population of sediment in the downstream direction (30).

1. California Debris Commission (1906) Map of the Yuba River California from the Narrows to its mouth in the Feather River. (The Commission, San Francisco, CA) Sheet 2. 1:9600.
2. James LA, Hodgson ME, Ghoshal S, Latiolais MM (2012) Geomorphic change detection using historic maps and DEM differencing: The temporal dimension of geospatial analysis. *Geomorphology* 137(1):181–198.
3. Stonestreet SE, Lee AS (2000) Use of LiDAR mapping for floodplain studies. *Building Partnerships—2000 Joint Conference on Water Resource Engineering, Planning, and Management* (US Army Corps of Engineers, Sacramento, CA).
4. Ghoshal S, James LA, Singer MB, Aalto R (2010) Channel and floodplain change analysis over a 100-year period: Lower Yuba River, California. *Remote Sensing* 2(7): 1797–1825, 10.3390/rs2071797.
5. Adler LL (1980) Adjustment of the Yuba River, California, to the influx of hydraulic mining debris, 1849-1979. PhD dissertation (University of California, Los Angeles).
6. Singer MB (2007) The influence of major dams on hydrology through the drainage network of the Sacramento Valley, California. *River Research and Applications* 23(1): 55–72.
7. Gilbert GK (1917) *Hydraulic-Mining Debris in the Sierra Nevada,* US Geological Survey Professional Paper (US Geological Survey, Menlo Park, CA), Vol 105.
8. Slater LJ, Singer MB (2013) Imprint of climate and climate change in alluvial riverbeds: Continental United States, 1950-2011. *Geology* 41(5):595–598.
9. Maurice-Bourgoin L, Aalto R, Guyot JL (2002) Sediment-associated mercury distribution within a major Amazonian tributary: Century-scale contamination history and importance of flood plain accumulation. *The Structure, Function and Management Implications of Fluvial Sedimentary Systems*, eds Dyer FJ, Thoms MC, Olley JM (IAHS Press, Wallingford, UK), pp 161–168.
10. Hunerlach MP, Alpers CN, Marvin-DiPasquale M, Taylor HE, DeWild JF (2004) *Geochemistry of Mercury and Other Trace Elements in Fluvial Tailings Upstream of Daguerre Point Dam, Yuba River, California, August 2001* (US Geological Survey, Reston, VA), US Geological Survey Scientific Investigations Report 2004-5165.
11. Olund SD, DeWild JF, Olson ML, Tate MT (2005) *Methods for the Preparation and Analysis of Solids and Suspended Solids for Total Mercury. Book 5-Laboratory Analysis, Techniques and Methods* (US Geological Survey, Reston, VA).
12. Simon A, Curini A, Darby SE, Langendoen EJ (2000) Bank and near-bank processes in an incised channel. *Geomorphology* 35(3-4):193–217.
13. Casacgli N, Rinaldi M, Gargini A, Curini A (1999) Pore water pressure and streambank stability: Results from a monitoring site on the Sieve River, Italy. *Earth Surf Process Landf* 24(12):1095–1114.

14. Amiri-Tokaldany E, Darby SE, Tosswell P (2003) Bank stability analysis for predicting reach scale land loss and sediment yield. *Journal of the American Water Resources Association* 39(4):897–909.
15. Selby MJ (1993) *Hillslope Materials and Processes* (Oxford Univ Press, Oxford).
16. Singer MB, Dunne T (2004) Modeling decadal bed-material flux based on stochastic hydrology. *Water Resour Res* 40(3):W03302, 10:1029/2003WR002723.
17. Knighton AD (1998) *Fluvial Forms and Processes* (Edward Arnold, London).
18. Singer MB, Dunne T (2006) Modeling the influence of river rehabilitation scenarios on bed material sediment flux in a large river over decadal timescales. *Water Resour Res* 42(12):W12415, 10.1029/2006WR004894.
19. Singer MB, Aalto R, James LA (2008) Status of the lower Sacramento Valley flood-control system within the context of its natural geomorphic setting. *Natural Hazards Review* 9(3):104–115.
20. Singer MB, Aalto R (2009) Floodplain development in an engineered setting. *Earth Surf Process Landf* 34(2):291–304.
21. Springborn M, Singer MB, Dunne T (2011) Sediment-adsorbed total mercury flux through Yolo Bypass, the primary floodway and wetland in the Sacramento Valley, California. *Sci Total Environ* 412-413:203–213.
22. Domagalski JL (2001) Mercury and methylmercury in water and sediment of the Sacramento River basin, California. *Appl Geochem* 16(15):1677–1691.
23. Hervouet JM (2000) TELEMAC modeling system: An overview. *Hydrol Processes* 14(13): 2209–2210.
24. Kilham NE (2009) Floodplain sedimentation on the Feather River, California: Combined use of remote sensing and numerical modeling to analyze contemporary deposition patterns in a historically mined basin. PhD dissertation (University of California, Santa Barbara, CA).
25. Krone RB (1993) Sedimentation revisited. *Nearshore and Estuarine Cohesive Sediment Transport*, ed Mehta AJ (American Geophysical Union, Washington, DC), pp 108–125.
26. van Rijn LC (1993) *Principles of Sediment Transport in Rivers, Estuaries and Coastal Seas* (Aqua Publications, Amsterdam).
27. Thonon I, Roberti JR, Middelkoop H, van der Perk M, Burrough PA (2005) In situ measurements of sediment settling characteristics in floodplains using a LISST-ST. *Earth Surface Processes and Landforms* 30(10):1327–1343.
28. Kilham NE, Roberts D, Singer MB (2012) Remote sensing of suspended sediment concentration during turbid flood conditions on the Feather River, California: A modeling approach. *Water Resour Res* 48(1):W01521.
29. James LA (1989) Sustained storage and transport of hydraulic gold mining sediment in the Bear River, California. *Ann Assoc Am Geogr* 79(4):570–592.
30. Aalto R, Nittrouer CA (2012) 210Pb geochronology of flood events in large tropical river systems. *Philos Trans A Math Phys Eng Sci* 370(1966):2040–2074.

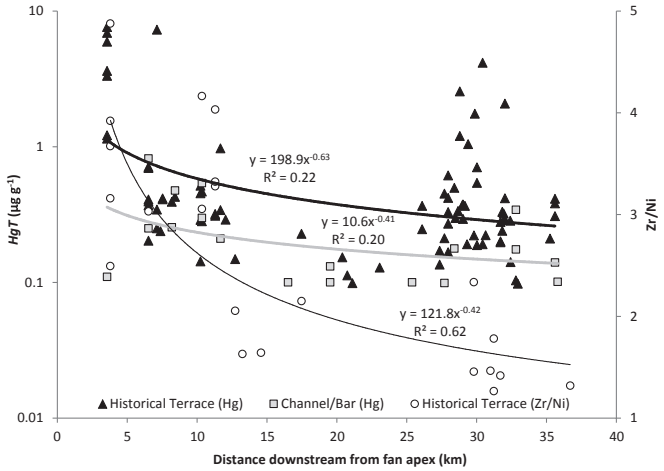

Fig. S1. Downstream relationships in HgT above background values and Zr/Ni through the Yuba Fan.

Table S1. Rates of degradation (feet per year) in the Lower Yuba Fan

Years	XS2	XS3	XS9	XS11	XS13
1899–1906		0.29	0.14	0.21	0.21
1906–1912	2.50	1.70	0.83	0.83	0.75
1912–1928	0.13		0.50	0.44	0.41
1928–1979	0.14	0.08	0.10	0.18	0.26

Historical rates of channel degradation in the thalweg at various cross-sections within the lower Yuba Fan are reproduced from the work of Adler (5). That dissertation may be accessed to see the location of each cross-section.

Dataset S1. HgT and Zr/Ni values, distances downstream, and spatial/geomorphic classifications

Dataset S1

Boldfaced sample codes indicate samples from recent deposits averaged to obtain a characteristic value of HgT used to model Hg fluxes (see above), which are presented in Fig. 4.